Exp Fluids (2013) 54:1581
DOI 10.1007/s00348-013-1581-8

RESEARCH ARTICLE

Experimental characterization of powered Fontan hemodynamics in an idealized total cavopulmonary connection model

Anna-Elodie M. Kerlo · Yann T. Delorme · Duo Xu · Steven H. Frankel · Guruprasad A. Giridharan · Mark D. Rodefeld · Jun Chen

Received: 5 February 2013 / Revised: 14 May 2013 / Accepted: 6 July 2013

Abstract A viscous impeller pump (VIP) based on the Von Karman viscous pump is specifically designed to provide cavopulmonary assist in a univentricular Fontan circulation. The technology will make it possible to biventricularize the univentricular Fontan circulation. Ideally, it will reduce the number of surgeries required for Fontan conversion from three to one early in life, while simultaneously improving physiological conditions. Later in life, it will provide a currently unavailable means of chronic support for adolescent and adult patients with failing Fontan circulations. Computational fluid dynamics simulations demonstrate that the VIP can satisfactorily augment cavopulmonary blood flow in an idealized total cavopulmonary connection (TCPC). When the VIP is deployed at the TCPC intersection as a static device, it stabilizes the four-way flow pattern and is not obstructive to the flow. Experimental studies are carried out to assess performance, hemodynamic characteristics, and flow structures of the VIP in an idealized TCPC model. Stereoscopic particle image velocimetry is applied using index-matched blood analog. Results show excellent performance of the VIP without cavitation and with reduction of the energy losses. The non-rotating VIP smoothes and accelerates flow, and decreases stresses and turbulence in the TCPC. The rotating VIP generates the desired low-pressure Fontan flow augmentation (0–10 mmHg) while maintaining acceptable stress thresholds.

A.-E. M. Kerlo · Y. T. Delorme · D. Xu · S. H. Frankel · J. Chen (✉)
School of Mechanical Engineering, Purdue University, West Lafayette, IN 47907, USA
e-mail: junchen@purdue.edu

A.-E. M. Kerlo
e-mail: akerlo@purdue.edu

G. A. Giridharan
Department of Bioengineering, University of Louisville, Louisville, KY 40292, USA

M. D. Rodefeld
Department of Surgery, Indiana University School of Medicine, Indianapolis, IN 46202, USA

1 Introduction

In a normal human heart, the right ventricle pumps deoxygenated systemic venous blood returning from the body to the lungs, and the left ventricle pumps oxygenated blood from the lungs to the body. In single ventricle congenital heart disease, one of the two ventricles fails to form in a way that is ever functional. It is the leading cause of death from any birth defect in the first year of life (Gillum 1994). In the most common variant, *Hypoplastic Left Heart Syndrome* (HLHS), the left ventricle fails to form. Surgical repair of HLHS commits the right ventricle to pump blood to the body and then through the lungs in series. Since there is no subpulmonary ventricle, pulmonary blood flow is driven by systemic venous pressure alone. This circulatory arrangement is known as a univentricular Fontan circulation (Fontan and Baudet 1971). After Fontan repair, a number of significant circulatory inefficiencies exist: the single ventricle is subjected to increased workload; the single ventricle is chronically preload deprived, decreasing cardiac output; systemic venous pressure is pathologically elevated. Current surgical repair consists of a complex series of three staged operations (Fig. 1) called *Staged Fontan palliation* and is notorious for post-operation complications and poor survival (50–70 %) (Ohye et al. 2010; Ashburn et al. 2003).

Published online: 28 July 2013

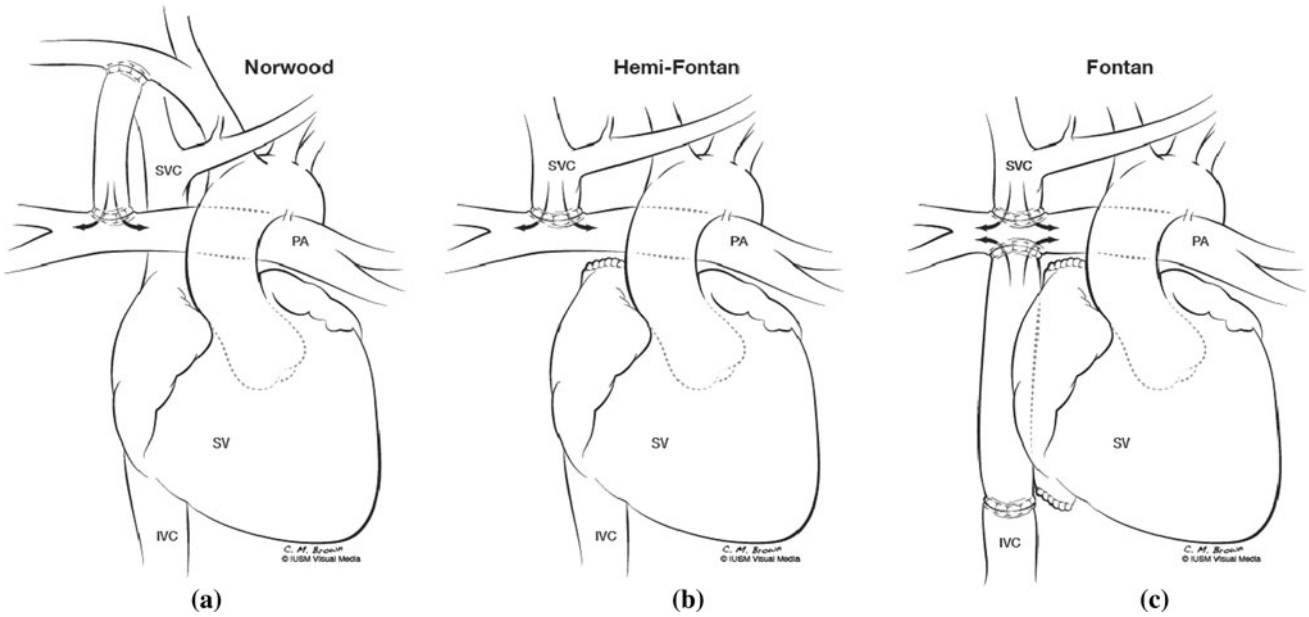

Fig. 1 Staged Fontan palliation of single ventricle. **a** Neonate: Stage-1 Norwood. High pressure flow to neonatal lungs is derived from a systemic-to-pulmonary artery shunt. **b** 4–6 months: Stage-2 Hemi-Fontan or Glenn. The Superior Vena Cava (*SVC*) is connected to the pulmonary artery as the sole source of pulmonary blood flow. Inferior Vena Cava (*IVC*) blood is ejected to the body. **c** 2–5 years: Stage-3 completion Fontan. *IVC* flow is diverted to the pulmonary artery to form a total cavopulmonary connection (*SV* single ventricle)

Although Fontan palliation has dramatically impacted survival of single ventricle heart disease (Rodefeld et al. 1996), serious early and late problems persist. The *univentricular Fontan circulation* is inherently inefficient and is prone to eventually fail (DeLeval 1998). With the lack of a subpulmonary ventricle, there is a simultaneous increase in the systemic venous pressure and a decrease in the pulmonary arterial pressure, a hydraulic deficiency which is referred to clinically as the *Fontan paradox* (Dasi et al. 2008; DeLeval 1998). The surgically constructed geometry of the right-sided circulation (where a subpulmonary ventricle is lacking) is a *total cavopulmonary connection* (TCPC), in which systemic venous blood must flow passively from the vena cavae (VC) into the pulmonary arteries (PA) via an orthogonal 4-way connection. This iatrogenic construction is not found elsewhere in nature. Inflow from the inferior and superior vena cavae (IVC and SVC) is bi-directionally opposed, as is outflow into the left and right pulmonary arteries (LPA and RPA). The TCPC has been a natural target to potentially improve Fontan circulatory inefficiency: it is generally accepted that any means to improve flow at this level would exponentially impact the circulation as a whole (Rodefeld et al. 2003).

From a bioengineering perspective, energy (head) loss in the TCPC occurs due to dissipation of the impinging venous inflows. Efforts have been made to optimize passive flow in the TCPC by altering its geometry. Migliavacca et al. (2003) studied a right/left offset between the IVC and SVC. Soerensen et al. (2007) and Marsden et al. (2009) have investigated solutions which split the IVC and/or SVC, to prevent the two inflows from colliding directly and thus reduce head losses. In either of these solutions, the pressure gain is modest, not exceeding 0.5–1 mmHg.

Alternatively, our group is pursuing a solution which will *actively* augment Fontan flow. A means to modestly augment (2–10 mmHg) TCPC flow would simultaneously reduce systemic venous pressure and increase pulmonary arterial pressure, thereby improving preload and cardiac output. It would enable clinical management of the single ventricle patient on the basis of normal biventricular physiology, dramatically improving quality and duration of life (Rodefeld et al. 2003, 2011; Ungerleider et al. 2004). We are designing a cavopulmonary assist device for both temporary and permanent support. The design has evolved from micro-axial pumps placed in the vena cavae (Rodefeld et al. 2003), to a folding propeller concept (Throckmorton et al. 2007), and finally to the current *viscous impeller pump* (VIP) (Kennington et al. 2011). Deployment of the VIP in the TCPC not only provides mechanical cavopulmonary support of all 4 flow axes of the TCPC with a single pump, but also has the critical failsafe advantage in that it reduces head losses when not rotating, as a passive flow diverter (Rodefeld et al. 2010).

The conceptual design of VIP is inspired by the Von Karman viscous pump (Karman 1921; Panton 2005). The latest design is a bi-conical impeller with surface vanes (Fig. 2). It was optimized by combining predictions from Reynolds-Averaged Navier-Stokes (RANS) computational

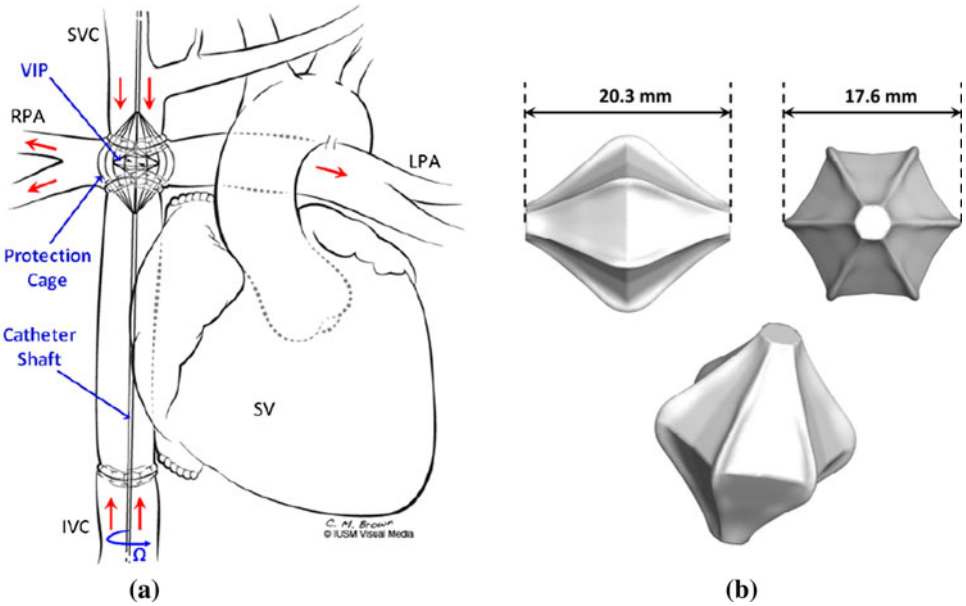

Fig. 2 **a** Powered Fontan circulation: deployment of VIP within TCPC. *Arrows* denote flow pathways. **b** The VIP design used in the present study

fluid dynamics (CFD) simulations and manufacturability constraints (Kennington et al. 2011). A prototype was tested for hemolysis with excellent results (Giridharan et al. 2013). RANS-based CFD simulations have been widely used to study cardiovascular flow and design medical devices. However, its predictions of powered Fontan hemodynamics must be validated by comparing with experimental data. In particular to this study, issues that must be addressed include: (a) Because TCPC hemodynamics involve complex and irregular flows, with streamline curvature, rotation, and possible transition to turbulence, RANS-based CFD has difficulties to accurately predict the secondary flow features (Khunatorn et al. 2003; Durbin and Reif 2010). (b) Blood flow in the TCPC is by nature transitional (Reynolds number, $Re = \rho UD/\mu$, of the order of hundreds, where D is the characteristic vessel diameter), so the use of turbulence models developed for high Re turbulence is under question for these simulations. (c) The capability of RANS-based CFD software (usually with second order accuracy) to simulate highly unsteady flow in TCPC is also questioned (Pekkan et al. 2005). The possible superiority of high-order large eddy simulation (LES) methods must be proven by comparison with experimental data. (d) The deployment of a rotating VIP at thousands of RPM in the TCPC makes the analysis of the problem even more complex. In this study, we characterize powered Fontan hemodynamics by studying the flow field induced by VIP in an in vitro TCPC setup. Flow features within the idealized TCPC model are investigated. Local flow patterns are visualized to predict potential areas of recirculation and high shear stress, which may lead to thrombogenicity and hemolysis. The results will be used to further improve the design of the VIP to achieve performance and flow specifications, in addition to validating CFD predictions.

This report is organized as follows: the experimental apparatus is described in Sect. 2; Sect. 3 introduces the measurement techniques; experimental conditions are summarized in Sect. 4; results are presented in Sect. 5. A summary is given, and the future research is discussed in Sect. 6.

2 Experimental setup

The experimental setup, shown in Fig. 3, consists of an in vitro idealized TCPC model connected to a mock circulation loop simulating single ventricle physiology, a viscous impeller pump driven by an externally mounted motor, and flow regulation system to handle index-matched fluid for optical measurements, as well as a supporting system.

2.1 Idealized TCPC model

An idealized TCPC model is built for in vitro experiments, as shown in Fig. 4d, where the two inlets (IVC and SVC) meet perpendicularly with the two outlets (LPA and RPA). The inside diameters of the inlets and outlets are $D = 22$ mm and $D_o = 18$ mm, respectively, representing the physiological SVC/IVC diameters (20–24 mm) and LPA/RPA diameters (16–20 mm) of typical adult patients. The intersection of the inlets and outlets is smoothed (curvature radius 10 mm) to exclude sharp corners, which mimics typical anatomy and adult Fontan patients. All the geometric details are identical to the computational domain used in CFD simulation (Delorme et al. 2013). The transparent TCPC models are constructed following an in-house procedure (Fig. 4): (1) use 3D printing technique to make a solid negative half mold of the idealized TCPC geometry; (2) create a 2-part marine silicone

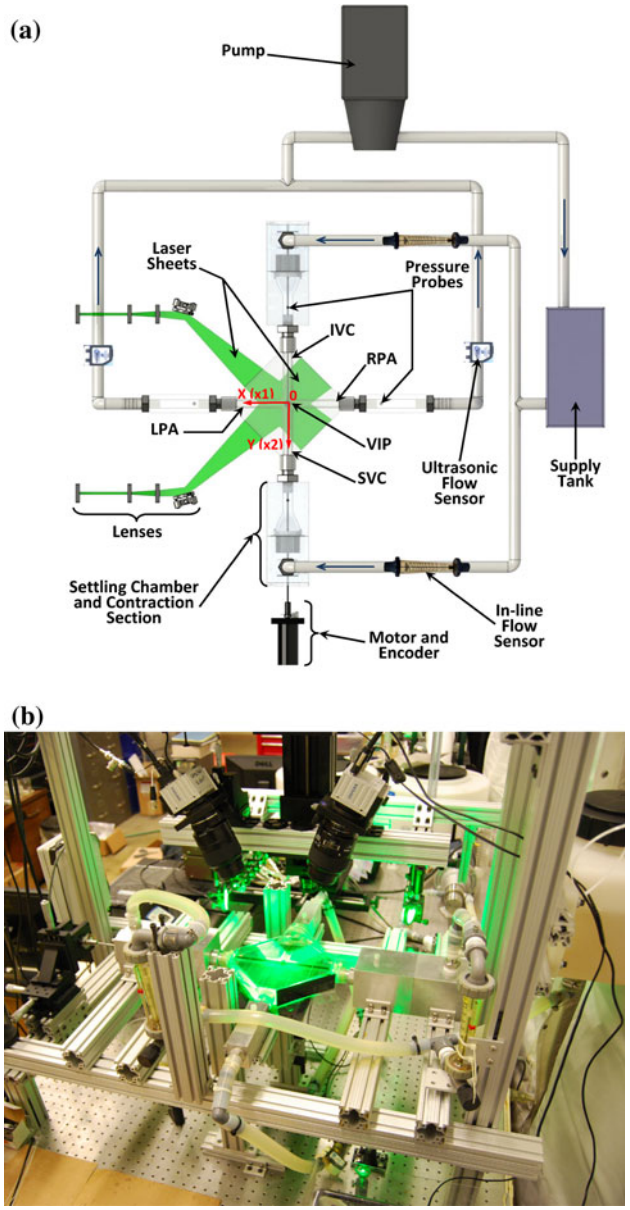

Fig. 3 **a** Schematics of the experimental setup with VIP and idealized TCPC model in a mock circulation loop. **b** Picture of the experimental setup. Figure does not show the entire circulation loop

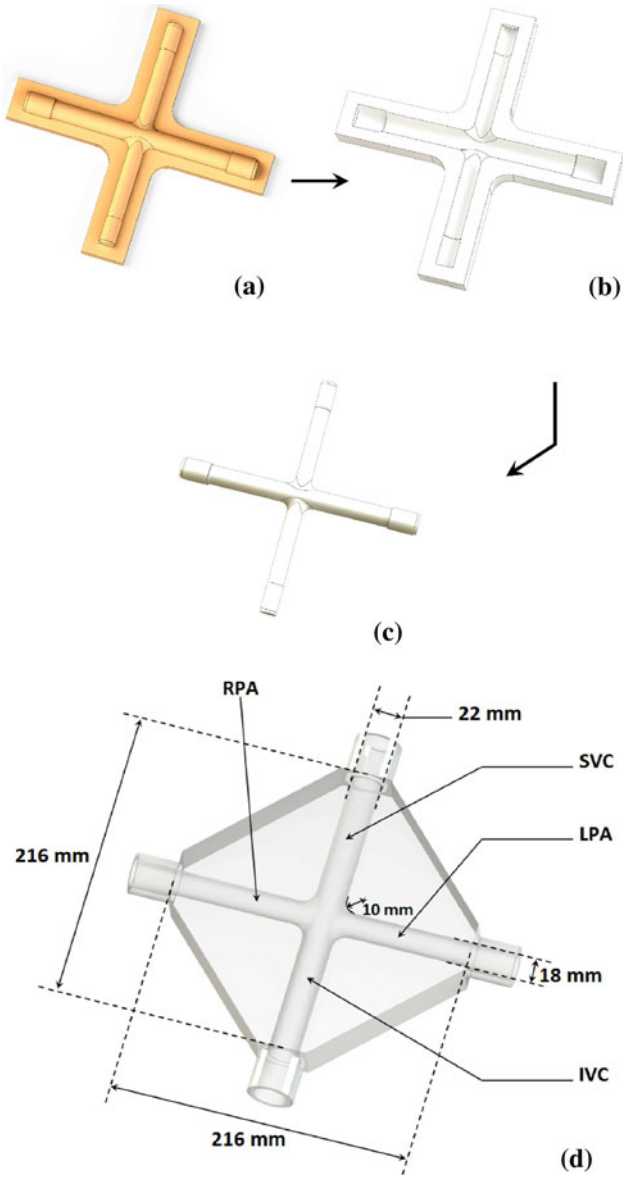

Fig. 4 Illustration of procedure to build the transparent silicone TCPC model: **a** 3D printed half mold, **b** marine silicone half mold, **c** wax negative mold, **d** transparent silicone test section (Sylgard 184) after wax is removed from inside

rubber mold from the negative 3D printed mold; (3) cast water soluble optical wax in the 2-part silicone mold. Surface of the negative mold is lightly sanded to provide a smooth finish; (4) encase the wax in transparent silicone rubber (Sylgard 184, Refractive Index $n = 1.417$); (5) remove the wax mold using warm water to evacuate the transparent TCPC model. The top and bottom surfaces of the TCPC model are flat and parallel to each other to ensure undistorted images in optical measurements. The four-side surfaces of the TCPC model are perpendicular to the top and bottom surfaces so that the laser sheet illuminates the test section without deflection. The accuracy of the dimensions of the model is determined by accuracy of the 3D printer, which is typically 0.2 mm. Dimensions of the inlets/outlets are verified after production using pin gages with precision of 0.00254 mm. The TCPC model is mounted into the circulation loop and the interfaces in such a way that the inner surface of the conduit remains smooth to avoid additional flow disturbance.

2.2 Viscous impeller pump

The impeller prototype is constructed of DSM 11122 XC Watershed material using stereolithography (SLA) techniques.

The VIP is a bi-conical disk shape structure with six surface vanes. The height of VIP is 20.3 mm, and its maximum diameter is 17.6 mm (Fig. 2b). The geometric details of this optimized prototype can be found in Kennington et al. (2011). A thin layer of polyurethane is coated on the surface to provide a finish mimicking the production material to be used and to protect the VIP from chemical degradation. A second layer of black primer is coated on the VIP to minimize surface reflection in optical measurement.

A Brushless DC-Servomotor (peak power 207 W, 202 mNm, Faulhaber) and a Servo Amplifier (BLD 5018, Faulhaber) are used to drive the VIP through a rigid stainless steel shaft (3.175 mm diameter). This combination can drive the VIP at an operational range from 1,000 to 7,000 RPM. To mimic the clinical application of the VIP where a catheter shaft enclosed in a protection sheath drives the VIP, and to avoid direct contact between the working fluid and the rotating shaft, the shaft is protected by a Garolite (G-10) sheath (outside diameter of 4.76 mm). The sheath is also coated with black primer to minimize surface reflection. An incremental encoder (Gurley 7700) is installed on the shaft to monitor the angular (phase) position of the VIP. A CMOS camera (DCC1645C, Thorlabs GmbH, resolution 1,280 × 1,024 pixels) is used to ensure accurate centering of the VIP in the TCPC model and is not used for acquiring PIV images.

2.3 Mock circulation loop

Both inlets of TCPC are connected to two identical settling chambers (Fig. 5). They are designed following the design principles of a low-speed wind tunnel (Bradshaw and Pankhurst 1964; Sykes 1977). In the settling chamber, a perforated plate is placed before a honeycomb plate (cell size ~3 mm and thickness 25.4 mm) and four layers of mesh screens to straighten the flow and reduce turbulence. A contraction section (area reduction ratio 3.31:1) further reduces the velocity fluctuations at the inlet of TCPC. This setting produces well-defined inlet boundary conditions with good experimental repeatability, which can be prescribed in CFD simulations. The shaft driving the VIP and the protection sheath are inserted through the settling chambers and are supported and sealed by a micro-bearing mounted on the external housing of the settling chamber.

The blood analog fluid used in the present study is a mixture of water, glycerin, and sodium iodide (46 %/33 %/21 % by weight). It mimics the dynamic viscosity of blood ($\mu \sim 4.15 \times 10^{-3}\,\mathrm{kg/m \cdot s}$) while matching the refractive index of the TCPC model (n = 1.417). The matched refractive indices of the TCPC model and the working fluid prevent distortion in optical experiments (discussed in Sect. 3). The fluid density is $\rho = 1{,}283\ \mathrm{kg/m^3}$, while typical blood density is about 1,060 kg/m^3. Refractive indices and fluid viscosity are chosen as more important parameters to be matched over the density in this experiment. The blood analog used in the present study has properties of a Newtonian fluid, whereas blood is a non-Newtonian shear thinning fluid. Differences in the measured flow field between non-Newtonian and Newtonian fluids can be significant under certain conditions, as documented in the literature (Gijsen et al. 1999; Chen and Lu 2004; Johnston et al. 2006; Hsu et al. 2009). The fluid temperature is controlled through the room temperature, which is kept constant. Before each data set acquisition, the fluid's refractive index and viscosity are fine-tuned to compensate for possible changes due to small room temperature fluctuations. After each data set is acquired, the fluid temperature is checked again to ensure constant refractive index and viscosity. The increase in temperature between the beginning and the end of a data set acquisition is less than 0.2 °C and does not affect significantly the refractive index or the viscosity.

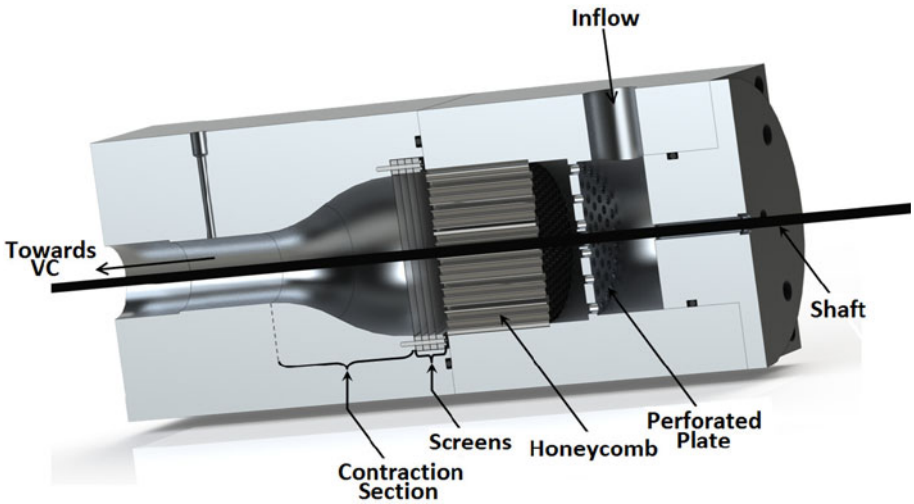

Fig. 5 Schematic of the settling chamber for generating stable inlet flow conditions

Blood flow is pulsatile in the arteries; when the blood reaches the capillary beds where it encounters the highest resistance, it becomes steady. As a result, the blood flow arriving at the TCPC via the VCs presents negligible pulsatility due to the contraction of the single ventricle. Thus, the flow in TCPC is assumed non-pulsatile in the present study. A constant flow centrifugal driver is magnetically coupled to a series CA centrifugal pump to circulate the fluid within the mock circulation loop. A baseline flow rate, $Q_o = 4.4$ L/min, generated in the loop is controlled by a pump controller via an in-house LabView program (through a National Instrument PXI 6221 DAQ). The resulting mean flow in the inlets is $U_o = 9.65$ cm/s. This yields a Reynolds number at the inlets of $Re = \rho U_o D/\mu \sim 656$. A supply tank connecting the pump and the inlets serves as a compliance chamber mimicking systemic compliance. The adjustable hydraulic head of the tank determines the preload on the TCPC model. Tubing clamps are placed on the flexible hoses to regulate and even the flow rates throughout the circulation loop, and to obtain a 50–50 % split of the flow at the two inlets and the two outlets.

3 Measurement techniques

3.1 Pressure and flow rate measurements

Four pressure ports are designed at each branch of the test section (IVC, SVC, LPA, and RPA, Fig. 3a) to house high fidelity Millar 5F pressure catheters (Millar Instruments, TX), whose accuracy is ±1 mmHg (133.322 Pa). The flows entering the inlets and exiting from the outlets are simultaneously measured using flow meters. This enables fine adjustment of flow rates in each branch of the TCPC model. Two inline flow meters are deployed at the inlets to achieve 50 %/50 % split. Two clamp-on tubing ultrasonic flow-sensors (PXL12, Transonic Systems Inc. accuracy ±5 %) and flowmeter modules (TS410 402-TT, Transonic Systems Inc.) are used for non-invasive measurement of the flow rate in the outlets (Fig. 3a).

3.2 Hemolysis study

Hemolysis is the breakdown of red blood cell (RBC) membranes, causing the release of hemoglobin and other components into the plasma. Because the RBCs carry the oxygen to the body, their breakage can lead to anemia. Hemolysis study of the VIP in an idealized TCPC geometry is performed following the procedure described by Giridharan et al. (2013). Fresh whole bovine blood is used in an in vitro loop to characterize the hemolysis induced by the VIP. Two sets of tests are performed. The VIP is operated at 5,000 ± 50 RPM against a pressure head of 7.5 ± 1 mmHg for the first set (8.5 ± 1 mmHg for the second set respectively), resulting in a flow rate of 8.1 ± 0.4 L/min (7.3 ± 0.4 L/min respectively). The normalized index of hemolysis (NIH) and the modified index of hemolysis (MIH) are calculated based on the American Society of Testing and Materials (ASTM) standards for each set and then averaged to obtain the final values. This hemolysis study, performed at the Cardiovascular Innovation Institute, University of Louisville (Louisville, KY), complies with Food and Drug Administration guidelines for 510(k) submission and ASTM standards (International 2005a, b).

3.3 Flow visualization

In order to observe the flow interactions within the TCPC model, flow visualization for the cases without the VIP and with the static VIP is conducted using water as the working fluid. Dye is injected at each inlet. Blue dye is used in the SVC, and red dye is used in the IVC. When the impeller rotates at thousands of RPM, the dyes are mixed quickly and the structures cannot be discerned, and thus, the results are not reported here.

3.4 Velocity measurement

A stereoscopic particle image velocimetry (SPIV) system is integrated into the setup to measure the three velocity components within different horizontal planes next to and

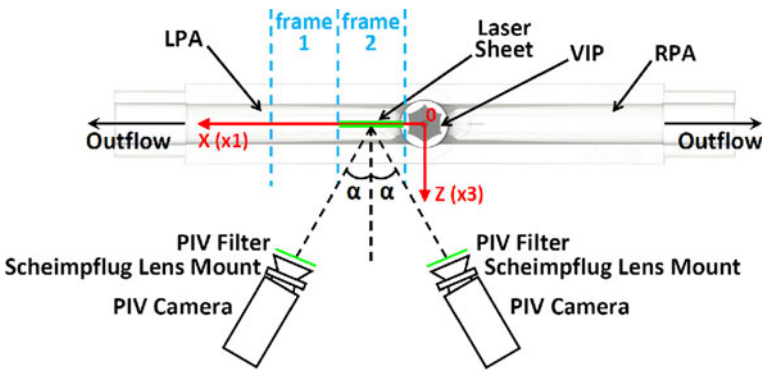

Fig. 6 Schematic of the SPIV experimental setup for the cases with the VIP

away from the VIP along one of the outlets (frames 1 and 2, Fig. 6). The origin of the coordinate system is set at the center of the VIP as shown in Figs. 3a and 6. The x-axis (x_1) is along the central axis of one outlet, and the y-axis (x_2) is along the central axis of one inlet.

Hollow glass beads (mean diameter 10 μm, specific gravity 1.1) are uniformly mixed in the working fluid as seeding particles. A dual-head Nd:YAG pulse laser (Quantel Twins BSL140, $\lambda = 532$ nm, peak energy 130 mJ/pulse, beam diameter of $\sim$6 mm) illuminates the central horizontal plane of the test section ($x - y$ plane) at a controlled time interval ΔT, between two consecutive pulses. The laser beam is split into two branches which are directed toward the area of interest, from two directions, using a combination of lenses and mirrors to convert the beam to a 1-mm-thick laser sheet (Fig. 3a). Two CCD cameras (Imperx IPX 2M30 LMCN, 8 bits) of 1,600 × 1,200 pixels resolution are mounted on two 3D translation stages, which are further mounted on another translation stage (Figs. 3b, 6). All images are recorded and transferred to a host laptop computer using an image grabber board and camera-link cables. Two Scheimpflug lens mounts interface the cameras and the lenses (105 mm focal length) to obtain focused images when the cameras point to the area of interest at tilt angle of $\alpha = 30°$. The cameras record the particle images at the area of interest under double exposure mode at a sampling rate of 5 Hz. The time delay between two pulses is set to 250–500 μs, depending on the mean flow velocities in the test section. The cameras and the laser are synchronized with a multi-channel pulse generator. An in-house LabView program is developed to control the pulse generator, the circulation loop, the VIP driving system and the flow-sensors.

In the present study, the SPIV setup is calibrated using a two-level calibration plate and following the Scheimpflug criterion: (1) the cameras are focused at the area of interest; (2) the cameras are translated up by 31 mm to focus at the calibration target submerged into the working fluid placed in a petri dish. The distance between the surface of the working fluid in the petri dish and the target submerged in the working liquid is kept identical to the one between the area of interest and the top surface of the TCPC model; (3) the calibration images are acquired, and the cameras are translated back to the original position to focus at the center plane of the TCPC model; and (4) the recorded calibration images are processed using a SPIV processing software (DaVis 8.1).

The recorded particle images are processed by a two-pass scheme: the first pass adopts an interrogation window of 64 × 64 pixels and 50 % overlap, and the second pass reduces interrogation window to 32 × 32 pixels and keeps a 50 % overlap.

A typical uncertainty estimate of the instantaneous PIV data is about 0.1 pixel, corresponding to a relative uncertainty of about 1 % for the in-plane components, u_1, and u_2 (for characteristic displacement of about 10 pixels). Similarly, the relative uncertainty for the out-of-plane component, u_3, is about 1.7 % for a tilt angle of $\alpha = 30°$. The uncertainties in the variables involving in-plane mean velocities, $\overline{u}_1$, and $\overline{u}_2$ are about 0.016 %, and those involving the out-of-plane velocity, $\overline{u}_3$, are about 0.027 % (ensemble set of 4,000 snapshots). The uncertainties in terms involving the r.m.s values are about 0.022 % for the in-plane velocities and 0.039 % for the out-of-plane velocity. The uncertainties involving velocity gradients are about 0.084 % for the in-plane velocities and 0.142 % for the out-of-plane velocity. Detailed discussions of PIV accuracy analysis are documented in the literature (Prasad 2000; Adrian and Westerweel 2010; Keane and Adrian 1990; Raffel et al. 2007).

4 Characterization of experimental conditions

SPIV measurements are conducted at two consecutive downstream locations along the central $x - y$ plane of the LPA outlet (frames 1 and 2, Fig. 7) with an area of interest of 30 × 22.5 mm^2. From each image pair, a total of 106 × 76 velocity vectors are resolved with a spatial resolution $\delta \approx 0.29$ mm. Data are also acquired at the central $x - y$ plane of SVC inlet to gain insight into the inlet boundary conditions (frame 0, Fig. 7). SPIV measurements are performed for four cases at different VIP rotation speed and a control case without the VIP installed, as summarized in Table 1. In the inlets and for the cases with the VIP, due to the presence of the shaft and protection sheath, as well as the axisymmetric nature of the inlet flow, data are only acquired in half of the inlet. For the control case with no VIP, the data are acquired in the entire inlet. For each case, N = 4,000 or 2,000 snapshots of velocity field are measured to form an ensemble set for statistical analysis.

In the following analysis, flow parameters are normalized using the inlet diameter D and the inlet mean velocity U_o. Unless otherwise mentioned, the following expressions use Einstein notation. The ensemble averaged velocities and the velocity fluctuations are calculated using the Reynolds decomposition:

$$\overline{u}_i(\mathbf{x}) = \frac{1}{N}\sum_i u_i(\mathbf{x}, t), \quad u_i'(\mathbf{x}, t) = u_i(\mathbf{x}, t) - \overline{u}_i(\mathbf{x}). \tag{1}$$

The mean velocity magnitude of the ensemble averaged velocities is

$$U = \sqrt{\overline{u}_i \cdot \overline{u}_i}. \tag{2}$$

Velocity gradients are computed using a fourth order finite-difference scheme and velocity at a PIV grid indexed by (m, n):

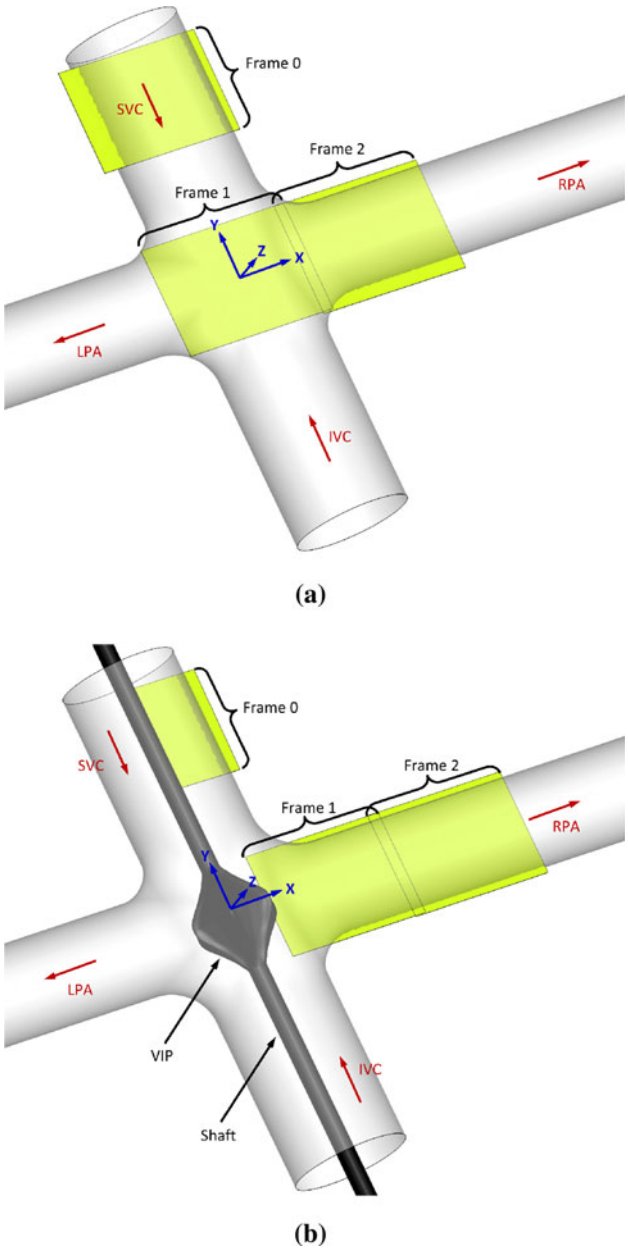

Fig. 7 Location of the data acquired: **a** case with no VIP (case 1) and **b** cases with VIP (cases 2, 3, and 4)

$$\left(\frac{\partial u_i}{\partial x_1}\right)_{m,n} = \frac{-u_{i_{m+2,n}} + 8u_{i_{m+1,n}} - 8u_{i_{m-1,n}} + u_{i_{m-2,n}}}{12\Delta x_1}, \tag{3}$$

$$\left(\frac{\partial u_i}{\partial x_2}\right)_{m,n} = \frac{-u_{i_{m,n+2}} + 8u_{i_{m,n+1}} - 8u_{i_{m,n-1}} + u_{i_{m,n-2}}}{12\Delta x_2}. \tag{4}$$

where $\Delta x_1 = \Delta x_2 = \delta$ in the present study. The averaged z-vorticity is

$$\overline{\omega} = \frac{\partial \overline{u}_1}{\partial x_2} - \frac{\partial \overline{u}_2}{\partial x_1}. \tag{5}$$

In addition, the averaged viscous shear stresses $\overline{\tau}_{ij}$ and the Reynolds stresses τ'_{ij} are computed from

Table 1 Summary of experimental conditions

Case description	1 No VIP (control)	2 Static VIP	3 Rotating VIP	4
			3,000 RPM	5,000 RPM
Baseline flow rate	$Q_o = 4.4$ L/min			
Mean flow (inlet)	$U_o = 9.65$ cm/s			
Dynamic viscosity of working fluid	$\mu \sim 4.15 \times 10^{-3}$ kg/m · s			
Density of working fluid	$\rho = 1.283 \times 10^3$ kg/m^3			
Reynolds number	$Re = \rho U_o D/\mu \sim 656$			
Refractive index of working fluid	$n = 1.417$			
SPIV spatial resolution	$\delta = 0.29$ mm			
Temperature of working fluid	22.9 °C	22.7 °C	22.8 °C	23.0 °C
	Center location of area of interest (x_c, y_c, z_c) (unit: cm)			
Frame 0 (inlet)	(0, 3.50, 0)	(0.55, 3.50, 0)	(0.55, 3.50, 0)	(0.55, 3.50, 0)
Frame 1	(0, 0, 0)	(2.21, 0, 0)	(2.43, 0, 0)	(2.43, 0, 0)
Frame 2	(2.88, 0, 0)	(4.83, 0, 0)	(5.10, 0, 0)	(5.10, 0, 0)
Number of velocity snapshots (N)	2,000	4,000	4,000	4,000

$$\overline{\tau}_{ij} = \mu\left(\frac{\partial \overline{u}_i}{\partial x_j} + \frac{\partial \overline{u}_j}{\partial x_i}\right), \tag{6}$$

and

$$\tau'_{ij} = -\rho\overline{u'_i u'_j}. \tag{7}$$

The turbulent kinetic energy is defined as half the trace of the Reynolds stress tensor

$$K = \frac{1}{2}\left(\overline{u'_i u'_i}\right). \tag{8}$$

To evaluate the potential for hemolysis induced by the flow, the scalar stress model proposed by Bludszuweit (1995) is employed

$$\sigma_{\text{scalar}} = \sqrt{\frac{1}{6}\Sigma\left(\sigma_{ii} - \sigma_{jj}\right)\left(\sigma_{ii} - \sigma_{jj}\right) + \Sigma\sigma_{ij}\sigma_{ij}}, \tag{9}$$

where

$$\sigma_{ij} = \overline{\tau}_{ij} + \tau'_{ij}. \tag{10}$$

The scalar stress formula does not use Einstein notation (repeated indices do not imply summation). Hemolysis is

caused by mechanical shear stresses which are sufficiently high to rupture the RBC membrane, or create pores in the RBC membrane (Fraser et al. 2012). In general, exposure to scalar stress less than 450 Pa for short durations is acceptable with respect to hemolysis. Our specification for the VIP design is scalar stress less than a threshold value, σ_T = 300 Pa, as in Blackshear et al. (1987), Forstrom and Blackshear (1970), etc. To apply this model, additional assumptions are needed as the derivatives in the z-direction cannot be calculated from the SPIV data. By continuity of incompressible flow, one has

$$\frac{\partial \overline{u}_3}{\partial x_3} = -\frac{\partial \overline{u}_1}{\partial x_1} + \frac{\partial \overline{u}_2}{\partial x_2}, \tag{11}$$

thus

$$\overline{\tau}_{33} = -(\overline{\tau}_{11} + \overline{\tau}_{22}). \tag{12}$$

In this paper, we also assume that the unresolved elements of velocity gradient tensor ($\partial u_i/\partial x_j$) are symmetric, i.e.,

$$\frac{\partial \overline{u}_1}{\partial x_3} \approx \frac{\partial \overline{u}_3}{\partial x_1}, \tag{13}$$

and

$$\frac{\partial \overline{u}_2}{\partial x_3} \approx \frac{\partial \overline{u}_3}{\partial x_2}. \tag{14}$$

This assumption arises from the fact that the known derivatives $\partial \overline{u}_2/\partial x_1$ and $\partial \overline{u}_1/\partial x_2$ have the same order of magnitude.

5 Results

5.1 Hydraulic performance test

The pressure rise P (evaluated by hydraulic head rise) induced by the VIP is a function of flow rate, Q, and rotation rate in the circulatory loop:

$$H = \frac{(P_{LPA} + P_{RPA})}{2g} - \frac{(P_{IVC} + P_{SVC})}{2g}. \tag{15}$$

Establishing the pressure–flow rate relationship ($H - Q$) is important for characterizing the hydraulic performance of VIP and other pumps. $H - Q$ measurements were performed at the Cardiovascular Innovation Institute, University of Louisville (Louisville, KY). The hydraulic performance of the VIP was evaluated in a mock circulation loop with in idealized TCPC as detailed in Kennington et al. (2011). Figure 8 shows $H - Q$ curves for a range of flow rates (0–8.2 L/min) and rotation rates (1,000–7,000 RPM) when the VIP and TCPC model are installed in the mock circulation loop.

The relative flatness of $H - Q$ curves demonstrates stable performance characteristics of the VIP over the full operational range (1,000–7,000 RPM): the VIP can provide stable pressure boost over a wide range of physiological conditions. The average slope of the profiles is about −0.427 mmHg/(L/min) for the different conditions tested. No cavitation is observed for the rotation speed range of the VIP up to 7,000 RPM. At 3,000 RPM and for flow rates from 0 to 3.5 L/min, a pressure augmentation from the vena cavae through the PAs of about 4 mmHg is observed. This modest pressure increase is in the ideal range to improve the Fontan circulation. At 5,000 RPM and for flow rates from 1 to 6 L/min, the pressure augmentation from the vena cavae through the PAs is of higher value (9–12 mmHg). 3,000–5,000 RPM is the expected nominal operational range for the VIP, but higher pressure flow may be necessary clinically if the patient presents with increased pressure head (pulmonary hypertension).

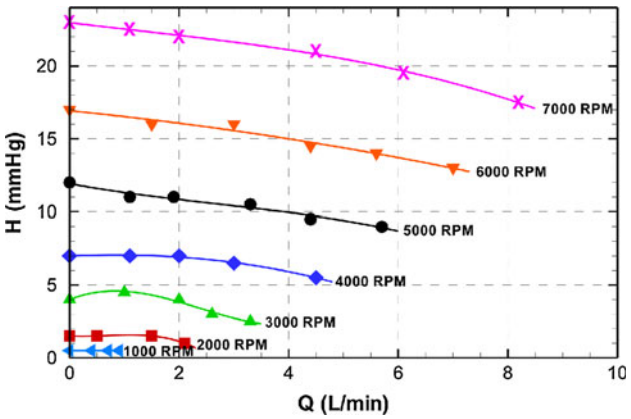

Fig. 8 Hydraulic performances of the VIP: pressure rise as a function of the flow rate in the mock loop and the rotation rate of the VIP

5.2 Hemolysis results

At the end of the 6-h testing period, the normalized index of hemolysis, is 0.036 ± 0.001 g/100 L for the first test set and 0.026 ± 0.001 g/100 L for the second test set, resulting in an averaged NIH of 0.031 ± 0.001 g/100 L. The modified index of hemolysis is 4.097 for the first test set and 3.437 for the second test set, resulting in an averaged MIH of 3.767. Hematocrit, red and white blood cell counts, and platelet counts over the 6-h period do not vary significantly from baseline. This hemolysis test demonstrates low hemolysis rate for the VIP.

5.3 Flow visualization results

5.3.1 No VIP

Figure 9 shows the flow visualization experiment for the no VIP case. The flow rate is constant at 4.4 L/min, and

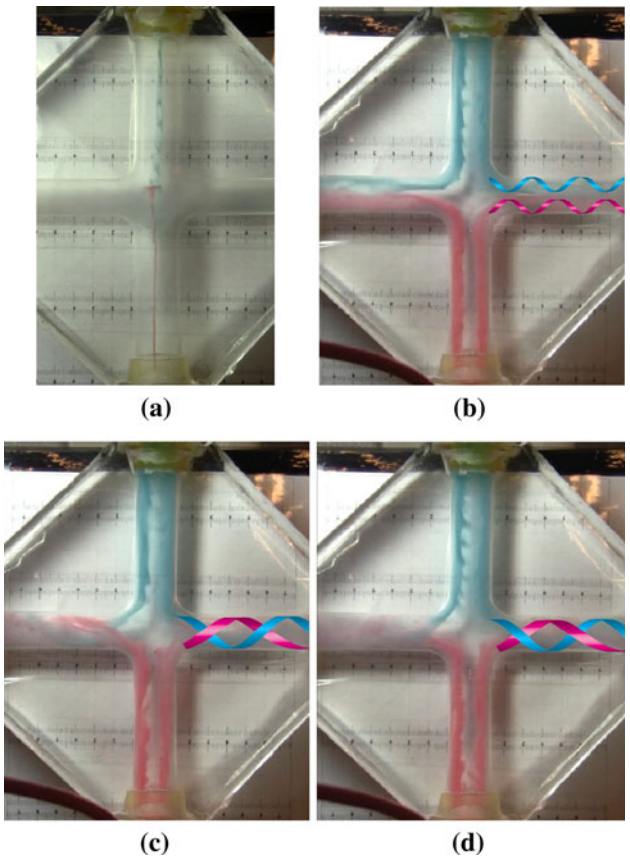

Fig. 9 Flow visualization snapshots for the case with no VIP **a** unstable stagnation point at the center of the TCPC, **b** two vortices in the PAs, **c** one vortex rotating clockwise in the PAs, **and d** one vortex rotating counter clockwise in the PAs

the flow split between each inlet is 50−50 %. The two impinging jets from the inlets create a stagnation point that oscillates in the center of the TCPC suggesting instabilities (Fig. 9a). A repetitive alternating pattern of one and two vortices along the PAs is observed (Fig. 9b–d). The two vortices come from each inlet; they are highly unstable and interact with each other until they merge forming a single vortex tube throughout the PAs. A single strong vortex induces more mixing than two smaller vortices, which is crucial to ensure a good hepatic factor distribution to the lungs. The hepatic factor is delivered to the venous blood by the liver, and its even distribution to both lungs is essential to prevent the development of pulmonary arteriovenous malformations (Pike et al. 2004). It is also observed that the vortex rotational direction alternates through time (Fig. 9c, d). This phenomenon is similar to the *swirl switching* phenomenon as it relates to the Dean vortices in turbulent pipe bent flows (Rutten et al. 2005) and is also observed in the large eddy simulations (LES) by Delorme et al. (2013).

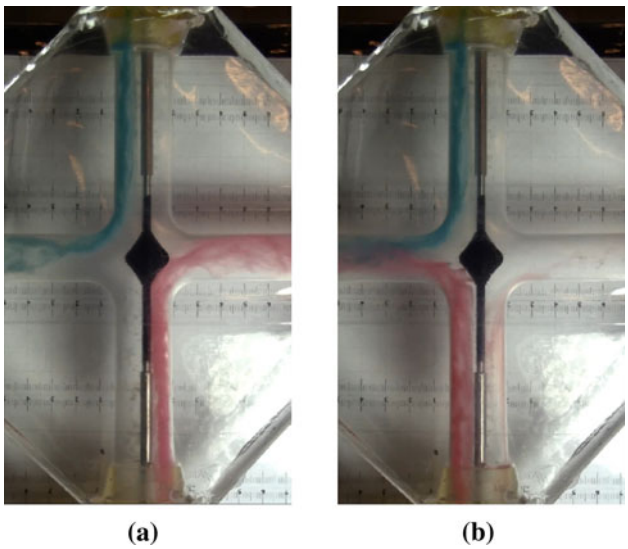

Fig. 10 **a**, **b** Flow visualization snapshots for case with static VIP

5.3.2 *Static VIP*

Figure 10 shows the flow visualization for the static VIP case. The flow rate is constant at 4.4 L/min, and the flow split between each inlet is 50−50 %. This figure shows that the VIP acts as a flow diverter and directs the flow from the inlet toward the outlets, preventing the collision of the two inlet jets. The flow is stable in the outlets, without the strong rotating vortex observed in the No VIP case.

5.4 Results from velocity measurements

Velocity measurements from SPIV in frame 0 are used to characterize the inlet boundary condition in the SVC and IVC of the TCPC model. Figure 11a–c shows the ensemble averaged v-velocity profiles for cases 1, 2, and 3, while Fig. 11d shows the ensemble averaged v-velocity profiles (left panel) and w-velocity profiles (right panel) for case 4 where the VIP rotates at 5,000 RPM. RMS values of the velocities are plotted as vertical bars. The u-velocity profiles are not plotted since they are virtually zero in all cases. For cases 1, 2, and 3, the w-velocity profiles are zero. A nearly parabolic v-profile is observed for the no VIP case, which is characteristic of laminar flow. This further justifies that imposed laminar (or weak turbulent) velocity inlet conditions can be adopted in the CFD simulations of flow in idealized TCPC without the VIP. The 0 RPM and 3,000 RPM cases show a similar pattern with the difference that the shaft and the protection sheath penetrate through the inlet. As a result, for the three cases with the VIP, the velocities are zero on the stationary sheath. The small imperfections in the v-component occurring at $x/D = \pm -0.1$ are attributed to the boundary layer

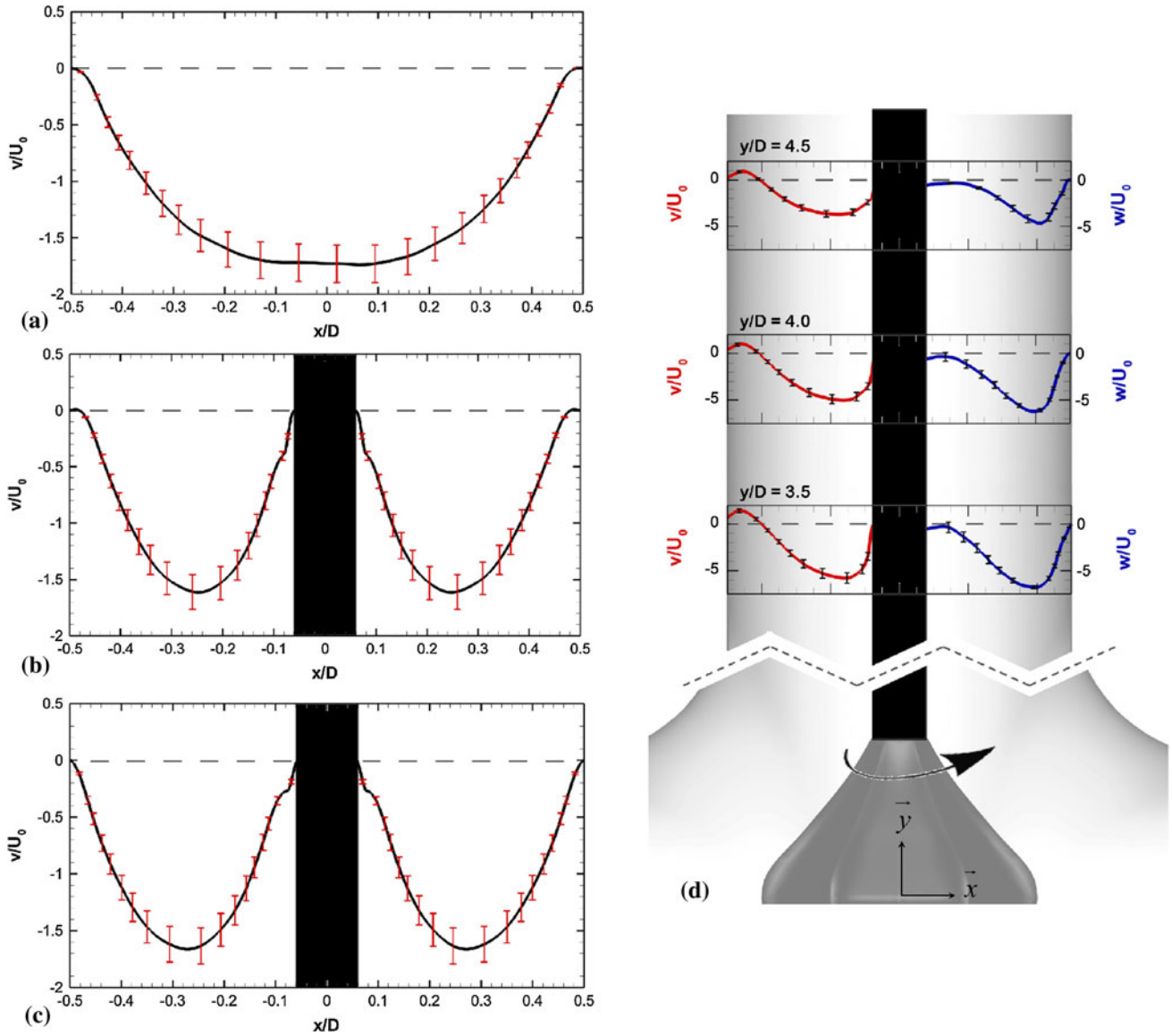

Fig. 11 Averaged velocity profiles at the inlet: **a** velocity in the *y* direction for the no VIP (case 1), **b** velocity in the *y* direction for the static VIP (case 2), **c** velocity in the *y* direction for the VIP rotating at 3,000 RPM (case 3), and **d** VIP rotating at 5,000 RPM (case 4) where velocity components in both *y* and *z* directions are plotted. *Vertical bars* represent the rms values of the measurements

development and separation along the stationary sheath (around rotating shaft). In addition, for these three cases, the velocity profiles in SVC and IVC do not show significant variation from $y/D \sim 5$ to $y/D \sim 3$, which suggests the inlet boundary conditions can be described by fully developed velocity profiles. For the 5,000 RPM case, the rotation of the VIP induces pre-rotation of the flow in the inlets: the *w*-velocity is not zero anymore, i.e., the flow is rotating around the *y*-axis. The absolute value of the peak value of *v*-profile increases as the flow travels closer to the VIP (as *y*/*D* decreases). Moreover, re-circulation is observed close to the wall, reflected by the fact that reverse flow (positive *v*) is observed from *v*-profile. The *u*-velocity (not presented) is equal to zero.

Figure 12 represents the ensemble averaged velocity fields. Figure 13 shows the averaged vorticity $\overline{\omega}$. Comparing results for cases 1 and 2 (no VIP and static VIP, Figs. 12, 13a, b), one can see that the VIP acts as a flow diverter and reduces vorticity compared to the case without VIP where the flows from the inlets are two confined impinging jets. The maximum velocity magnitude is similar for these two cases. Secondary helical patterns are observed in the mean flow of cases 1, 3, and 4, as highlighted in Fig. 12. In case 2 where the flows from two inlets are directed toward the outlets, this helical pattern is not observed. The flow fields created by the rotating VIP are highly three-dimensional. Figures 12 and 13 show significant recirculation zones in the outlet

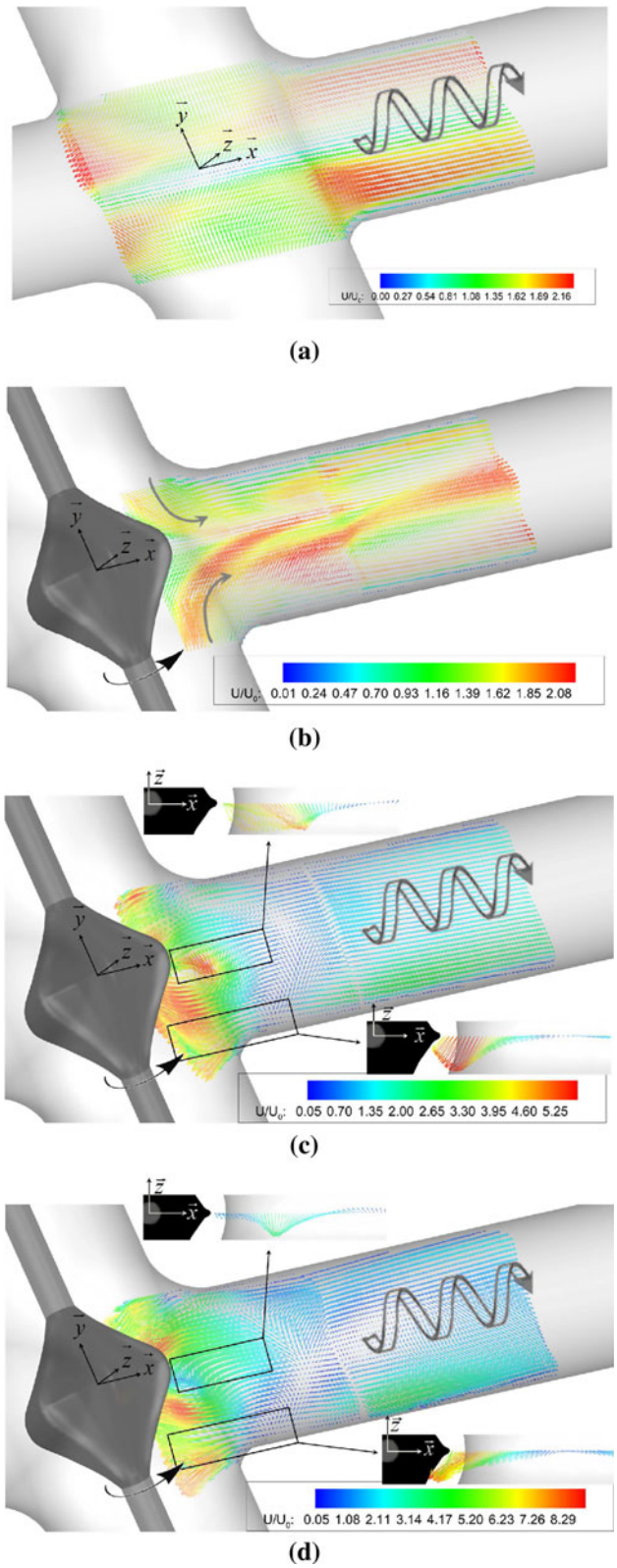

Fig. 12 Ensemble 3D velocity vectors $(\overline{u}, \overline{v}, \overline{w})$ colored by velocity magnitude: **a** no VIP, **b** static VIP, **c** VIP rotating at 3,000 RPM, and **d** VIP rotating at 5,000 RPM. Only 1/4 of the vectors are displayed for clarity

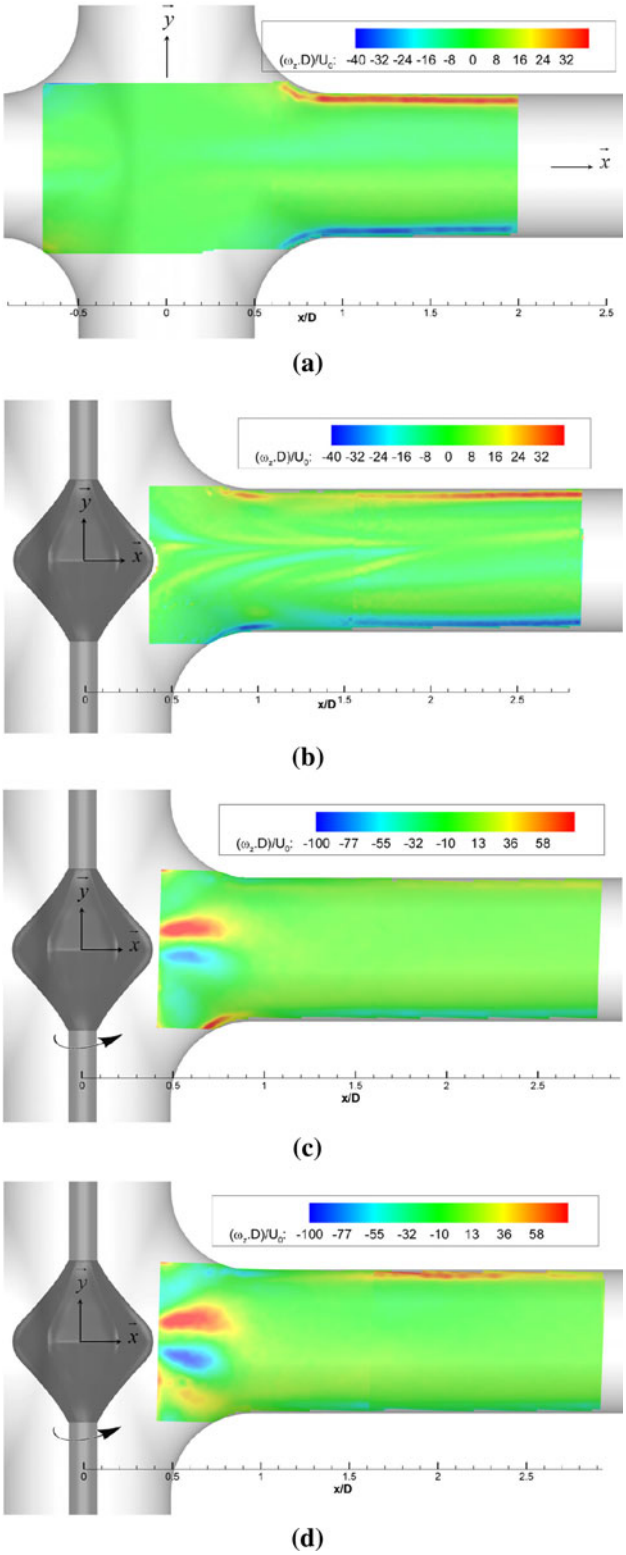

Fig. 13 Ensemble averaged z-vorticity $\overline{\omega}_z$: **a** no VIP, **b** static VIP, **c** VIP rotating at 3,000 RPM, and **d** VIP rotating at 5,000 RPM

close to the VIP when the VIP rotates. The recirculation of the flow close to the VIP happens in the same direction as the rotation of the VIP (from $\vec{z}$ to $\vec{x}$). The portion of the flow close to the inlets re-circulates toward the VIP until $x/D \approx 1$. It then switches direction and starts flowing toward downstream of the outlet. The portion of the flow around $y = 0$ travels toward the outlet until $x/D \approx 0.5$. It switches direction to flow toward the VIP between $x/D \approx 0.5$ and $x/D \approx 1$, before switching back to flow toward downstream of the outlet.

Figure 13c, d shows substantial out-of-plane motion in the vicinity of the VIP.

To further quantify the flow structure development in the outlets, the profiles of $\bar{u}, \bar{v}$ and $\bar{w}$, at five characteristic downstream locations, are plotted in Fig. 14 and compared for the four cases studied. For the cases without VIP and static VIP, the $\bar{u}$-velocity profiles do not show significant variation along the x-axis in the outlet when $x/D > 1.5$, similar to the profile of turbulent pipe flow (Pope 2006). Moreover, the presence of the static VIP makes the transition region short, enabling the flow to reach a developed state faster than without it. For the cases with the rotating VIP, at $x/D = 0.8$, the axial components of the mean flow follow a negative–positive–negative pattern across the cross section of the outlet, suggesting recirculation zones. This corroborates the observations made by examining averaged flow field (Fig. 12). As early as $x/D = 1.2$, the u-velocity profile develops toward a trend similar to the no VIP u-velocity profile, indicating that the effect of the VIP on the flow is limited to the close vicinity of the VIP. The $\bar{v}$-profiles for the no VIP case and static VIP case tend toward zero. For the rotating VIP cases, at $x/D = 0.8$, the $\bar{v}$-profiles highlight a negative–positive–negative–positive behavior. This pattern corroborates a behavior observed in the high-order Large Eddy Simulation of Powered Fontan Hemodynamics from Delorme et al. (2013), where also observed is the interaction of vortical structures along the LPA. As early as $x/D = 1.2$, the $\bar{v}$-velocities for the rotating VIP cases decrease and tend toward zero. For the cases without the VIP (respectively with the rotating VIP), the cross plane velocities ($\bar{w}$-velocity) follow a negative–positive (respectively positive–negative) pattern, which indicates stable helical flow. The static VIP shows a positive–negative–positive–negative pattern, which is again in agreement with the LES prediction from Delorme et al. (2013).

Turbulent characteristics of the flow in the TCPC are also of keen interest. Figure 15 gives the distribution of the turbulent kinetic energy (K) in frames 1 and 2. For the no VIP case, the plot shows higher turbulence region along the y-axis, where the two jets from each inlet impinge on each other. The existence of this high turbulence region indicates strong energy dissipation due to the collision of the two jets. The flow is less turbulent in the presence of the stationary VIP by an estimated 75 % compared to the case without the VIP. On the other hand, the rotating VIP induces more turbulent flow compared to cases 1 and 2. When rotating at 3,000 RPM (respectively 5,000 RPM), the flow patterns are more turbulent by an estimated 5,000 % (7,500 % respectively) at the maximum close to the VIP ($x/D \leq 0.8$). As early as $x/D = 1.2$, the turbulent kinetic energy decreases and tends toward levels similar to the no VIP case.

Figure 16 shows the Reynolds shear stresses, τ'_{xy}. This figure suggests that τ'_{xy} is significantly reduced and tends toward zero for the stationary VIP case compared to the case without the VIP. On the other hand, the rotating VIP induces more subsequent Reynolds stresses close to the VIP, compared to the case without the VIP. When rotating at 3,000 and 5,000 RPM, τ'_{xy} increases by about 4,000 and 6,000 %, respectively, at maximum (close to the VIP). The maximum Reynolds stress observed is around 50 Pa for the cases with the VIP rotating. The high stress region is in the close vicinity of the VIP, and the Reynolds shear stresses drop rapidly further downstream of the VIP.

Figure 17 shows that the averaged viscous shear stresses, $\overline{\tau}_{xy}$, analyzed according to Eq. 6, have the same order of magnitude for all four cases. The rotating VIP induces more viscous shear stresses compared to the no VIP case close to the VIP. When rotating at 3,000 and 5,000 RPM, $\overline{\tau}_{xy}$ increases by a factor of 2 and 4 at maximum, respectively. At $x/D = 1.2$ for these two cases, the levels of $\overline{\tau}_{xy}$ are comparable to the one of no VIP case. It is important to note the physically accurate behavior of the flow for all cases: across the cross section of the outlet, maximum values of $\overline{\tau}_{xy}$ occur close to the walls ($y = \pm 1/2D_o$). The near VIP region highlights significantly lower viscous shear stresses than Reynolds shear stresses. Due to the resolution of the SPIV data ($\delta \approx 0.29$ mm) and the use of finite-difference schemes to calculate velocity gradient (Eqs. 3, 4), the viscous shear stresses are estimated at a scale larger than approximately 1 mm. The contribution to viscous stresses from turbulence at unresolved scales may affect the uncertainty associated with blood damage estimations.

Figure 18 represents the scalar stresses, normalized by σ_T. First, for the cases without the VIP and with the static VIP, the scalar stresses are below the limit allowed: the maximum scalar stress observed is about 5 % of σ_T for the no VIP case and 2.5 % of σ_T for the static VIP case. This demonstrates lower scalar stress (and thus less hemolysis) in the presence of the stationary VIP compared to the case without the VIP. Hence, hemolysis is not a concern for these two cases. On the other hand, the rotating VIP induces more subsequent scalar stresses. The high stress

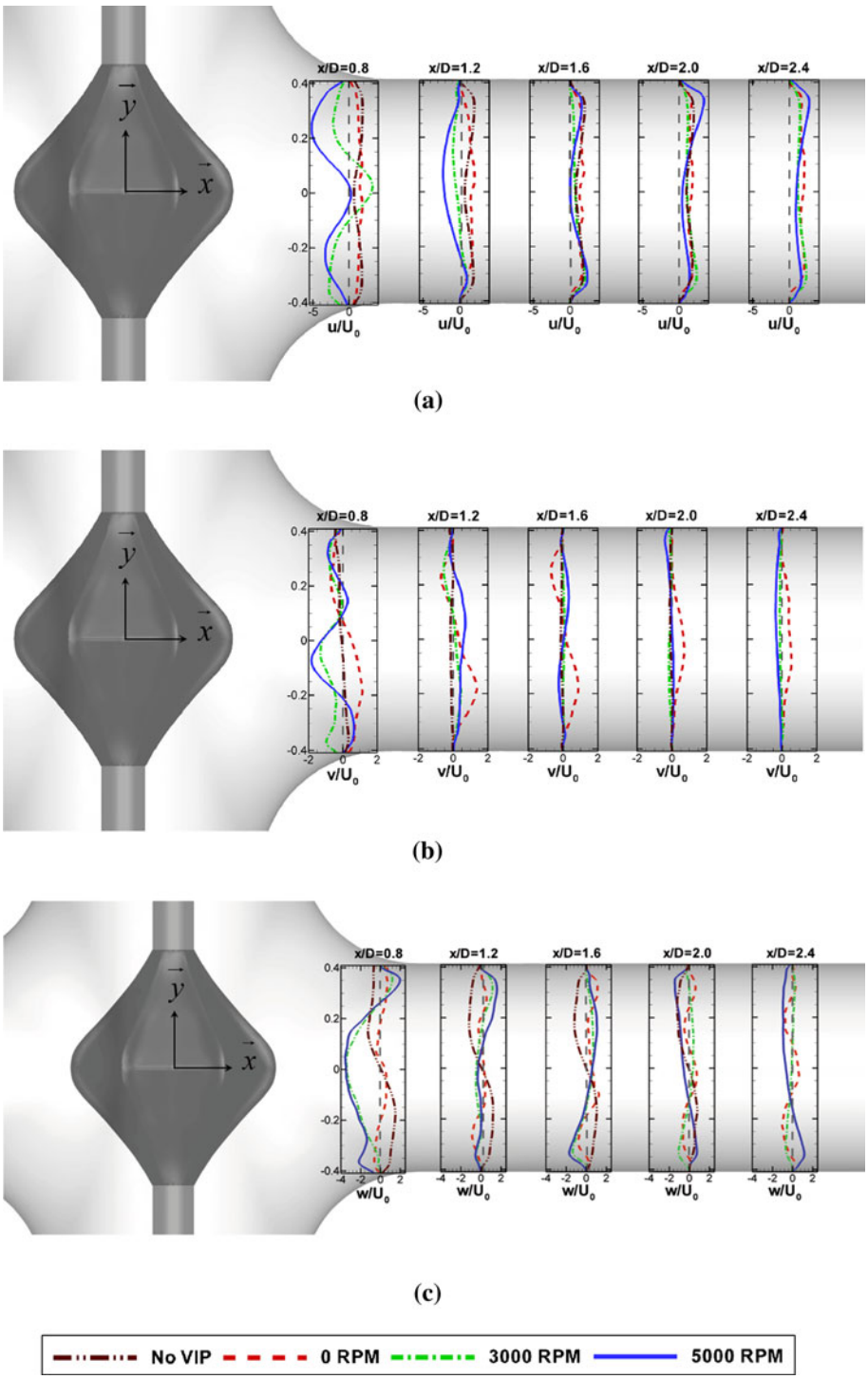

Fig. 14 Ensemble averaged velocity profiles of all four cases presented: **a** $\bar{u}$-profile, **b** $\bar{v}$-profile, and **c** $\bar{w}$-profile. Note that there is no "No VIP" profile for $x/D = 2.4$

region is limited to the near VIP region, and values as high as $3.3\sigma_T$ are reached for the VIP rotating at 5,000 RPM. However, σ_{scalar} decreases rapidly further downstream ($\sigma_{scalar} < \sigma_T$ at $x/D = 0.8$), suggesting the effect of the VIP on hemolysis is limited to a region localized around the VIP. The red blood cells experience high shear during a short period of time due to the high advection velocity in this region (Fig. 14), and thus, the hemolysis potential falls into an acceptable range. These predicted values of scalar stresses are higher than the low NIH values obtained by hemolysis testing with bovine blood as presented in Sect. 5.2. However, it is important to note that due to the assumptions made to estimate the shear stresses and the imperfect blood damage model used (Apel et al. 2001),

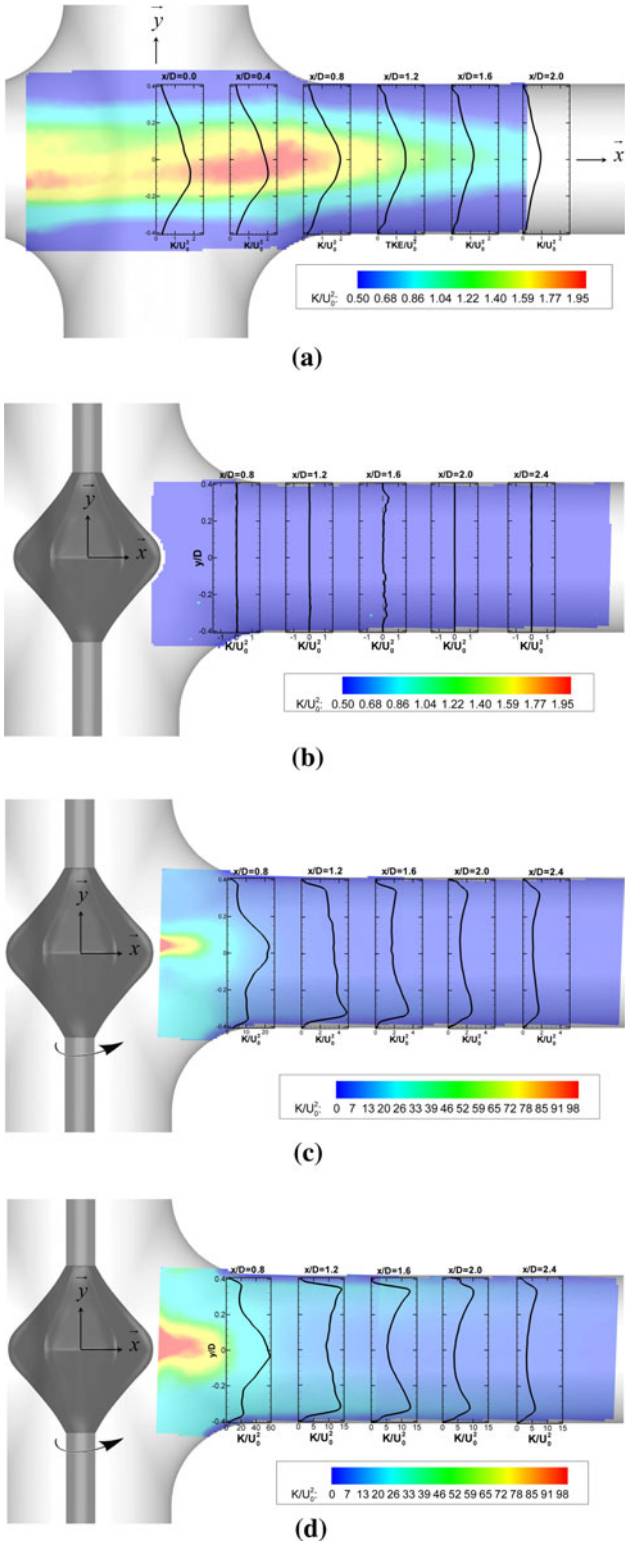

Fig. 15 Distribution of turbulent kinetic energy K: **a** no VIP, **b** static VIP, **c** VIP rotating at 3,000 RPM, and **d** VIP rotating at 5,000 RPM

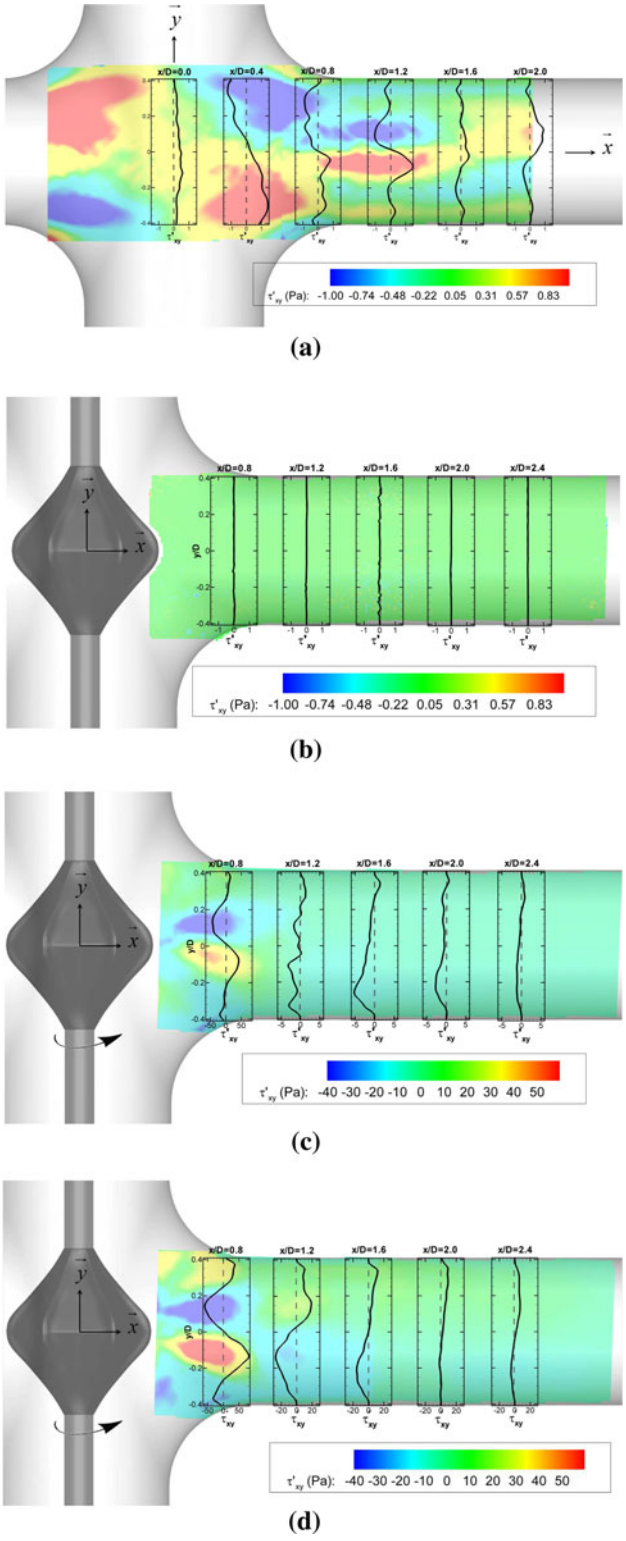

Fig. 16 Reynolds shear stresses, τ'_{xy}: **a** no VIP, **b** static VIP, **c** VIP rotating at 3,000 RPM, and **d** VIP rotating at 5,000 RPM. One is reminded that the scales for horizontal axes in (**c**) and (**d**) are adjusted for better presentation of the trends

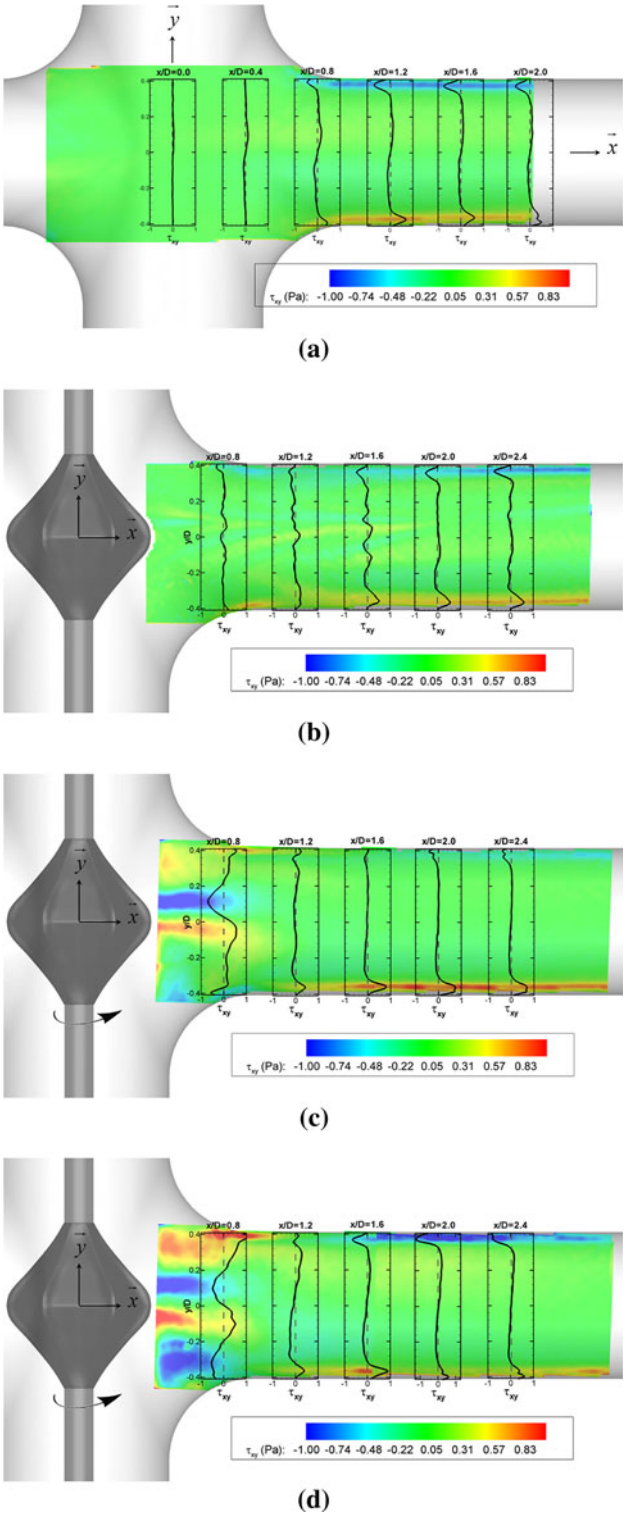

Fig. 17 Ensemble averaged viscous shear stresses, $\overline{\tau}_{xy}$: **a** no VIP, **b** static VIP, **c** VIP rotating at 3,000 RPM, and **d** VIP rotating at 5,000 RPM

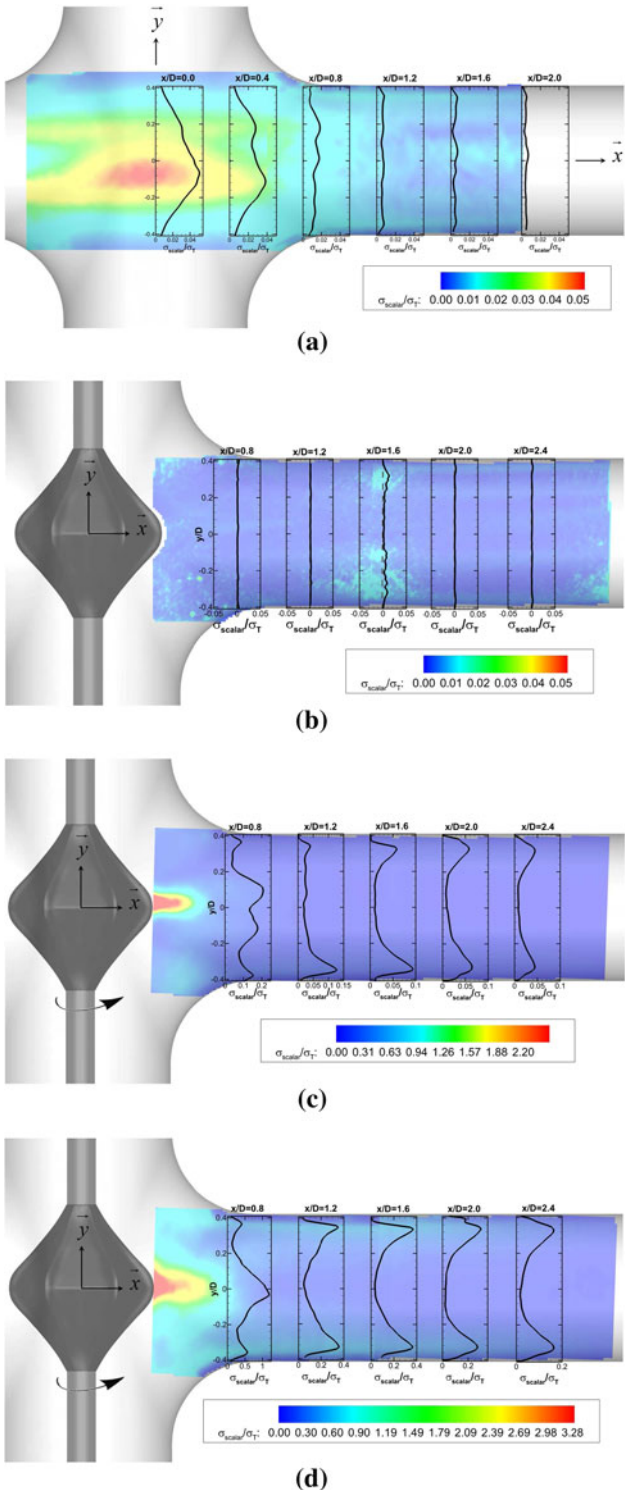

Fig. 18 Scalar stresses σ_{scalar} normalized by σ_{T}: **a** no VIP, **b** static VIP, **c** VIP rotating at 3,000 RPM, and **d** VIP rotating at 5,000 RPM

these scalar stresses results represent a rough estimation of the induced hemolysis. They provide qualitative assessment of the potentially critical flow regions.

6 Conclusions

We describe an experimental procedure to study flows in an idealized TCPC in vitro model with and without the

deployed VIP. The facility enables us to (1) produce physiological flow conditions using a blood analog fluid; (2) characterize the performance of VIP in idealized TCPC model by examining $H - Q$ characteristics; (3) characterize VIP potential for induced blood damage by hemolysis testing with bovine blood; (4) visualize the flow field within this complex geometry; (5) apply SPIV techniques to measure the 3D flow field along the outlets of the TCPC model; (6) characterize the development of mean flow field and turbulence in this TCPC–VIP combination; (7) compare the flow field between an idealized non-assisted TCPC (no VIP) and an assisted idealized TCPC (with the VIP); and (8) study potential blood damage using velocity data.

The findings in this study support this blood pump design in several respects. First, VIP performance is relatively insensitive to flow rate such that it is able to provide nearly stable cavopulmonary assist under different physiological conditions. At 5,000 RPM, the obtained pressure rise only decreases by 3 mmHg when the baseline flow rate increases from 2 to 6 L/min. In clinical applications, differences in physiological conditions (e.g., exercise vs. rest) imply different inlet conditions and flow rate variations. Cavitation over the VIP operational range is not observed. Energy losses associated with the TCPC are reduced by the presence of the non-rotating and rotating VIP. The non-rotating VIP smoothes flow and decreases stresses and turbulence in the TCPC. Thus, even the "failure mode" of the VIP is beneficial compared to the case without the VIP. The rotating VIP generates the desired low-pressure Fontan flow augmentation, while maintaining acceptable shear stress levels. Although the rotating VIP creates subsequent re-circulation zones and estimated scalar stresses are higher than the allowed threshold when $x/D < 1$, the measured NIH is low, suggesting that this blood pump has low hemolytic potential.

This study establishes a benchmark experimental data set for investigating the efficacy of different CFD technologies to predict cardiovascular flows with a transitional Reynolds number range, with and without a rotating device. Both inlet and downstream development of the flow structures are characterized in terms of averaged parameters such as turbulent kinetic energy, Reynolds stresses, and mean shear stresses. This data set is used to validate the predictions of high-order LES of idealized TCPC, as precisely documented by Delorme et al. (2013).

On-going experimental characterization of the flow induced by the VIP in the TCPC, including detailed flow structures and hemodynamic performances, is conducted to minimize risk of platelet activation, hemolysis, and thrombosis while maximizing hydraulic performance. Other current efforts include a study of the offset of the VIP in the TCPC in order to assess performance in cases where the vena cava axes are offset. Particle tracking is also being performed to calculate residence time and to determine the risk of platelet activation (Bluestein et al. 1997).

Acknowledgments Funding was provided in part by *National Institutes of Health* grants HL080089 and HL098353, and by an *American Heart Association Predoctoral Fellowship* (11PRE 7840073) (A.E.K.). The authors would also like to acknowledge Michael A. Sobieski RN, CCP and Steven C. Koenig of University of Louisville for their help with hemolysis testing.

References

Adrian RJ, Westerweel J (2010) Particle image velocimetry. Cambridge University Press

Apel J, Reinhard P, Sebastian K, Thorsten S, Helmut R (2001) Assessment of hemolysis related quantities in a microaxial blood pump by computational fluid dynamics. Artif Organs 25(5): 341–347

Ashburn DA, McCrindle BW, Tchervenkov CI, Jacobs ML, Lo GK, Bove EL, Spray TL, Williams WG, Blackstone EH (2003) Outcomes after the norwood operation in neonates with critical aortic stenosis or aortic valve atresia. J Thorac Cardiovasc Surg 125:1070–1082

Blackshear PL, Blackshear GL, Skalak R (1987) Handbook of bioengineering. Mc-Graw-Hill, New-York, chap Mechanical Hemolysis

Bludszuweit C (1995) Three-dimensional numerical prediction of stress loading of blood particles in a centrifugal pump. Artif Organs 19(7):590–596

Bluestein D, Niu L, Schoephoerter R, Dewanjee MK (1997) Fluid mechanics of arterial stenosis: relationship to the development of mural thrombus. Ann Biomed Eng 25(2):334–356

Bradshaw P, Pankhurst RC (1964) The design of low-speed wind tunnels. Prog Aerosp Sci 5:1–69

Chen J, Lu X (2004) Numerical investigation of the non-newtonian blood flow in a bifurcation model with a non-planar branch. J Biomech 37(12):1899–1911

Dasi LP, Pekkan K, Katajima HD, Yoganathan AP (2008) Functional analysis of fontan energy dissipation. J Biomech 41(10):2242–2252

DeLeval MR (1998) The fontan circulation: what have we learned? What to expect? Pediatr Cardiol 19(4):316–320

Delorme YT, Anupindi K, Kerlo AM, Shetty D, Rodefeld MD, Chen J, Frankel SH (2013) Large eddy simulation of powered fontan hemodynamics. J Biomech 46:408–422

Durbin P, Reif BP (2010) Statistical theory and modeling for turbulent flows, 2nd edn. Wiley, New York

Fontan F, Baudet E (1971) Surgical repair of tricuspid atresia. Thorax 26(3):240–248

Forstrom RJ, Blackshear GL (1970) Needles and hemolysis. N Engl J Med 283:208–209

Fraser K, Zhang T, Taskin ME, Griffith BP, Wu ZJ (2012) A quantitative comparison of mechanical blood damage parameters in rotary ventricular assist devices: shear stress, exposure time and hemolysis index. J Biomech Eng 134(8):081,002

Gijsen FJH, Allanic E, Vosse FNVD, Janssen JD (1999) The influence of the non-newtonian properties of blood on the flow in large arteries: unsteady flos in a 90 curved tube. J Biomech 32:705–713

Gillum RF (1994) Epidemiology of congenital heart disease in the united states. Am Heart J 127:919–927

Giridharan GA, Koenig SC, Sobieski MA, Kennington J, Chen J, Frankel SH, Rodefeld MD (2013) Performance evaluation of a pediatric viscous impeller pump for fontan cavopulmonary assist. J Thorac Cardiovasc Surg 145(1):249–257

Hsu C, Vu H, Kang Y (2009) The rheology of blood flow in a branched aterial system with three dimensional model: a numerical study. J Mech 25(4):N21–N24

International A (2005a) Astm f1830-97: standard practice for selection of blood for in vitro evaluation of blood pumps. West Conshohocken, PA

International A (2005b) Astm f1841-97: standard practice for assessment of hemolysis in continuous flow blood pumps. West Conshohocken, PA

Johnston BM, Johnston PR, Corney S, Kilpatrick D (2006) Non-newtonian blood flow in human right coronary arteries: transient simulations. J Mech 39(6):1116–1128

Karman TV (1921) Uber laminare und turbulente reibung. J Appl Math Mech/Zeitschrift fur Angewandte Mathematik und Mechanik 1(4):233–252

Keane RD, Adrian RJ (1990) Optimization of particle image velocimeters. part 1: double pulsed systems. Meas Sci Technol 1:1202–1215

Kennington JR, Frankel SH, Chen J, Koenig SC, Sobieski MA, Giridharan GA, Rodefeld MD (2011) Design optimization and performance studies of an adult scale viscous impeller pump for powered fontan in an idealized total cavopulmonary connection. Cardiovasc Eng Technol J 2(4):237–243

Khunatorn Y, Shandas R, DeGro C, Mahalingam S (2003) Comparison of in vitro velocity measurements in a scaled total cavopulmonary connection with computational predictions. Ann Biomed Eng 31(7):810–822

Marsden A, Bernstein A, Reddy M, Shadden S, Spilket R, Chan F, Taylor C, Feinstein J (2009) Evaluation of a novel y-shaped extracardiac fontan baffle using computational fluid dynamics. J Thorac Cardiovasc Surg 137:394–403

Migliavacca F, Dubini G, Bove E, DeLeval M (2003) Computational fluid dynamics simulations in realistic 3d geometries of the total cavopulmonary anastomosis: the influence of the inferior vena cava anastomosis. J Biomech Eng 125:805–813

Ohye RG, Sleeper LA, Mahony L, Newburger JW, Pearson GD, Lu M, Goldberg CS, Tabbutt S, Frommelt PC, Ghanayem NS (2010) Comparison of shunt types in the norwood procedure for single-ventricle lesions. N Engl J Med 362(21):1980–1992

Panton RL (2005) Incompressible flow, 3rd edn. Wiley, New York

Pekkan K, de Zelicourt D, Ge L, Sotiropoulos F, Frakes D, Fogel M, Yoganathan A (2005) Physics driven cfd modeling of complex anatomical cardiovascular flows—a tcpc case study. Ann Biomed Eng 33(3):284–300

Pike NA, Vricella LA, Feinstein JA, Black MD, Reitz BA (2004) Regression of severe pulmonary arteriovenous malformations after fontan revision and "hepatic factor" rerouting. Ann Thorac Surg 78:697–699

Pope SB (2006) Turbulent flows. Cambridge University Press, Cambridge

Prasad AK (2000) Stereoscopic particle image velocimetry. Exp Fluids (29):103–116

Raffel M, Willert CE, Wereley ST, Kompenhans J (2007) Particle image velocimetry: a practical guide. In: Experimental fluid mechanics, 2nd edn. Springer, New York

Rodefeld M, Boyd J, Myers C, LaLone B, Bezruczko A, Potter A, Brown J (2003) Cavopulmonary assist: circulatory support for the univentricular fontan circulation. Ann Thorac Surg 76: 1911–1916

Rodefeld M, Frankel S, Giridharan G (2011) Cavopulmonary assist: (em)powering the univentricular fontan circulation. Ann Thorac Surg 4(1):45–54

Rodefeld MD, Bromberg BI, Schuessler JP, Boineau JP, Cox JL, Huddleston CB (1996) Atrial flutter after lateral tunnel construction in the modified fontan operation: a canine model. J Thorac Cardiovasc Surg 111:514–525

Rodefeld MD, Coats B, Fisher T, Giridharan GA, Chen J, Brown JW, Frankel SH (2010) Cavopulmonary assist for the univentricular fontan circulation: Von karman viscous impeller pump. J Thorac Cardiovasc Surg 140(3):529–536

Rutten F, Schroder W, Meinke M (2005) Large-eddy simulation of low frequency oscillations of the dean vorticies in turbulent pipe bend flows. Phys Fluids 17(3):035,107–11

Soerensen D, Pekkan K, DeZelicourt D, Sharma S, Kanter K, Fogel M, Yoganathan A (2007) Introduction of a new optimized total cavopulmonary connection. Ann Thorac Surg 83:2182–2190

Sykes DM (1977) A new wind tunnel for industrial aerodynamics. J Wind Eng Ind Aerodyn 2(1):65–78

Throckmorton A, Ballman K, Myers C, Litwak K, Frankel SH, Rodefeld MD (2007) Mechanical cavopulmonary assist for the univentricular fontan circulation using a novel folding propeller blood pump. Am Soc Artif Intern Organs 53:734–741

Ungerleider RM, Shen I, Yeh T, Schultz J, Butler R, Silberbach M, Giacomuzzi C, Heller E, Studenberg L, Mejak B, You J, Farrel D, McClure S, Austin EH (2004) Routine mechanical ventricular assist following the norwood procedure improved neurologic outcome and excellent hospital survival. Ann Thorac Surg 77(1): 18–22